

Understanding the Effect of pH on the Solubility and Aggregation Extent of Humic Acid in Solution by Combining Simulation and the Experiment

Tu Lan, Peng Wu, Ziyi Liu, Martin Stroet, Jiali Liao, Zhifang Chai, Alan E. Mark,* Ning Liu,* and Dongqi Wang*



Cite This: <https://doi.org/10.1021/acs.est.1c05938>



Read Online

ACCESS |

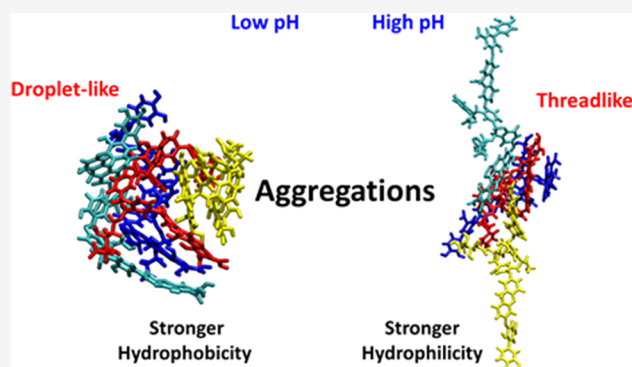
Metrics & More

Article Recommendations

Supporting Information

ABSTRACT: Molecular dynamics (MD) simulations were performed to investigate the dynamics of humic acid (HA) in an aqueous solution and the influence of pH, temperature, and HA concentration. The HA model employed in MD simulations was chosen and validated using experimental chemical composition data and Fourier transform infrared (FTIR) spectra. The simulations showed that the HA molecule has a strong propensity to adopt a compact conformation in water independent of pH, while the aggregation of HA was found to be pH-dependent. At high pH, the ionized HAs assembled into a thread-like structure, maximizing contact with water. At low pH, the neutral HAs formed a droplet-like aggregate, minimizing contact with the solvent. The simulation results are consistent with experimental data from dynamic light scattering (DLS) measurements and transmission electron microscopy (TEM) imaging. This work provides new insight into the folding and aggregation of HA as a function of pH and a molecular-level understanding of the relationship between the acidity and the structure, solubility, and aggregation of HA, with direct implications for HA-based remediation strategies of contaminated sites.

KEYWORDS: humic acid (HA), acidity, solubility, folding, aggregation, mechanisms, simulation and experiment



1. INTRODUCTION

Humic acids (HAs) are a class of natural organic compounds that belong to the family of humic substances (HSs). They are defined by being readily soluble in strongly basic solutions but less soluble at low pH following from the extraction protocols. This differentiates them from other HSs, namely, humin, which is defined by being insoluble, and fulvic acid, which is defined by being preferentially soluble at low pH.¹ HAs are widely distributed in soils, sediments, and natural water sources, and play a critical role in the sequestration of metal ions and hydrophobic organic contaminants (HOCs) in the natural environment. Typical functional groups found in HA include carboxyl, carbonyl, hydroxyl, phenolate, and aromatic rings. This diverse composition enables HA to be amphiphilic and exhibits a strong propensity to interact with metal ions and HOCs in soils and groundwater.^{1,2} These properties have led to growing interest in the role of HAs playing in the movement of various contaminants within soils and sediments and their potential use in the remediation of contaminated sites.

The experimental characterization of the interaction between HSs and inorganic/organic substances at the molecular level is challenging even using the most advanced experimental techniques. For this reason, theoretical methods

have been increasingly used to shed light on these systems as high-performance computing facilities have become more accessible.^{3–12} In a recent series of studies,^{13,14} we demonstrated that molecular dynamics (MD) simulations could be used to represent the dynamics of HA–uranyl–carbon nanotube (CNT)/graphene oxide (GO) ternary systems, where the CNT and GO represent alternative hydrophobic and amphiphilic surfaces, respectively. These works provided insights into the transformation of a surface from hydrophobic to hydrophilic via a noncovalent interaction with HA. Zhu et al.¹⁵ simulated the coaggregation of asphaltenes with Leonardite humic acid (LHA) and suggested that HA plays a key role in the fate and transport of oil contaminants. They also found that the presence of LHA promoted asphaltene aggregation and decreased the diffusion coefficient of asphaltenes in all simulated systems. Oostenbrink

Received: September 2, 2021

Revised: December 9, 2021

Accepted: December 16, 2021

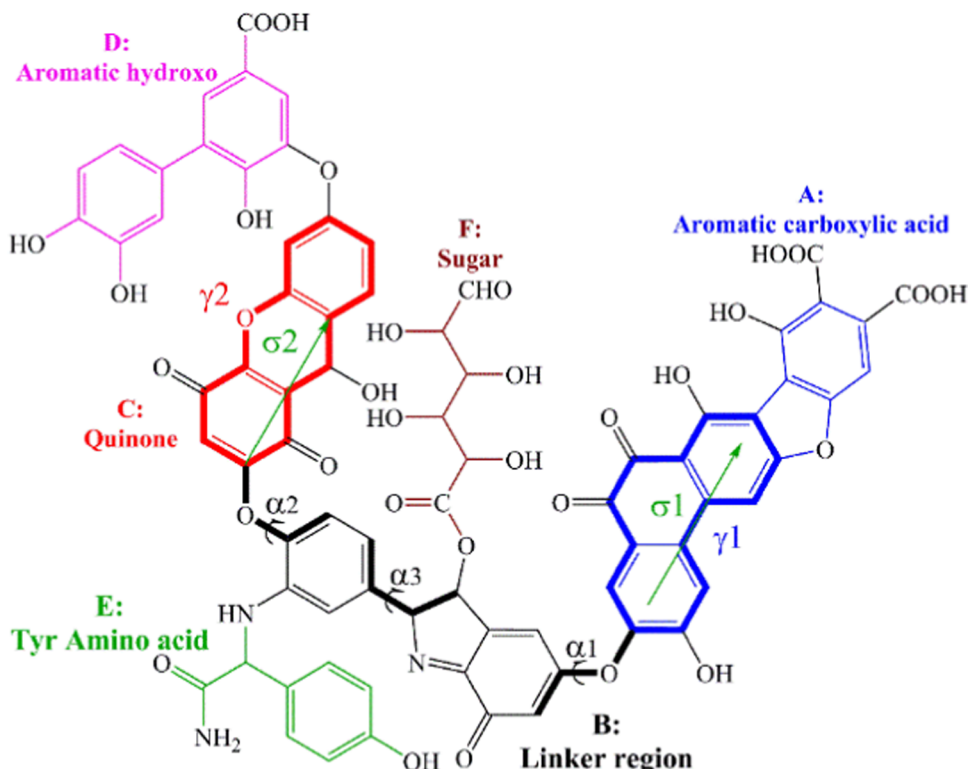


Figure 1. Molecular structure of HA according to the Stevenson model used in this work. The angle between two vectors (σ_1 and σ_2 in green, denoted as $V1$), the two planes (γ_1 in bold blue and γ_2 in bold red, denoted as $P1$), and the three dihedral angles (α_1 , α_2 , and α_3 , denoted as $D1$) were used as folding descriptors. The model was divided into six structure units based on functional groups: A: aromatic carboxylic acid (blue); B: linker region (black); C: quinone (red); D: aromatic hydroxo (purple); E: tyr amino acid (green); and F: carbohydrate (brown).

and co-workers developed an online tool, the Vienna Soil Organic-Matter Modeler, for convenient preparation of model HA systems in the condensed phase for use in computer simulations.^{16,17} Their work on the structure and dynamics of standard LHA was able to reproduce a range of experimental data.¹⁸ Although the structure of HA is expected to play a crucial role in determining its interaction with metal ions and HOCs, few of the existing experimental or theoretical studies related to HA have focused on the structure and dynamics of HA itself.^{18–22} In fact, knowledge of the structure of HAs is a key prerequisite to being able to first predict and then ultimately manipulate the properties of HAs used in environmental remediation applications, which is the underlying motivation for this work.

In this study, MD simulations have been used to investigate the effect of pH, temperature, and HA concentration on the folding and aggregation of HA in an aqueous solution. The results from the simulations were validated using dynamic light scattering (DLS) measurements and transmission electron microscopy (TEM) imaging, which also offered further insights into the state of HA aggregation at different pH values. The structural model used to represent HA was based on that proposed by Stevenson,¹ which was selected following an analysis of the chemical composition of purified HA used for the experimental studies. This work provides an atomic-level insight into the folding and aggregation behavior of HA. The potential implications for HA-based remediation strategies of contaminated sites are also discussed.

2. MATERIALS AND METHODS

2.1. Experiments. **2.1.1. Purification and Characterization of HA.** The HA was purchased from Real & Lead Chemical Co., Ltd. and purified by the procedure proposed by the International Humic Substance Society (IHSS) with minor modifications.^{23,24} Analytical reagents were used without further purification. The C, H, and N contents were determined by a Flash EA 1112 elemental analyzer (Thermo). Infrared spectra were recorded in the range of 500–4000 cm⁻¹ using a Nicolet 6700 Fourier transform infrared (FTIR) spectrometer (Thermo). The number of carboxylic acidic groups and total acidity of the HA sample were obtained by calcium acetate and barium hydroxide methods, respectively.¹ The number of phenolic acidic groups was calculated from the difference between the total acidity and the number of carboxylic acidic groups. The carbonyl and quinonyl groups were determined by potentiometric titration using a TitraMate 20 potentiometric titrator (Mettler Toledo, Switzerland).

2.1.2. DLS Measurements and TEM Imaging. The aggregation kinetics of HA under acidic (pH 2.5) and near-neutral (pH 7.8) conditions were determined using DLS techniques on a Zetasizer Nano ZS90 instrument (Malvern, U.K.) at 298 K. The NaAc–HAc (pH 2.5) and Tris–HCl (pH 7.8) buffers used in this work were prepared with deionized water. For each sample, 0.50 mL of the buffer was introduced into a quartz cell, followed by 0.50 mL of the HA solution (100 mg/L) dissolved in the same buffer. The resultant HA samples with a mass concentration of 50 mg/L were divided into two parallel groups, and three were used for DLS measurement and one for TEM imaging, respectively. They were measured after 120 s and left standing for a total of 3600 s (1 h) to ensure the

completion of the aggregation process. The surface morphologies of the HA before and after aggregation were examined using a Tecnai G2 F20 S-TWIN TEM (FEI). The aggregated HA samples were obtained after 12 h. TEM samples of HAs at two different pH values (2.5 and 7.8) were prepared by dropping 0.1 mL of a solution containing a HA mass concentration of 50 mg/L on copper grids. To maintain as much as possible of the original features of the HA aggregates, the copper grids containing the samples were flash-frozen in liquid nitrogen before being freeze-dried.

2.2. Molecular Dynamics Simulations. **2.2.1. Models and Systems.** The HA model ($C_{76}H_{49}N_3O_{32}$, Figure 1) proposed by Stevenson¹ was used in this work. This specific structure is in good agreement with the elemental composition and functional group content in the HA samples used in the experimental analysis, as shown in Section S1 of Supporting Information (SI). This model contains a range of hydrophobic and hydrophilic functional groups typically found in HA, including aromatic rings, aromatic carboxyl, phenolic hydroxyl, quinone, oxygen bridge, amino acid residue, and carbohydrate groups. Note, although the HA model contains a mixture of acidic, polar, and apolar groups, these are distributed across the molecule, meaning that the molecule would not be considered amphiphilic in the same way as many surfactants. Nevertheless, its flexible backbone can enable it to fold and become more or less amphiphilic depending on the environment.

Starting from the basic Stevenson model for HA (Figure 1), two alternative charge states were examined: one ionic and the other neutral. In the ionized model (named IHA), all carboxylate groups were deprotonated and the amine group was protonated. This yielded a molecular structure with 158 atoms and a net negative charge of $-2\ e$, representing HA in a near-neutral solution. In the neutral model (named NHA), because of the potential combinatorial problem in assigning which two of the three carboxylate groups were to be protonated or deprotonated, all titratable groups (the three carboxylate groups and the amine) were modeled in their neutral forms. NHA was used to represent the behavior of HA in an acidic solution and for comparison with IHA. A total of six systems were prepared differing in the type and the number of HA molecules. These are shown along with the simulation temperature in Section S2 of SI. The first three systems involved one molecule of IHA or NHA in the aqueous phase at a specific temperature (I1A, N1: 300 K; I1B: 350 K). These were constructed to investigate the effect of pH and temperature on the folding of HA. The last three systems (I4, N4, and M4) contained four HA molecules with different charge states. These were used to qualitatively evaluate the influence of the HA concentration and to investigate the aggregation of HAs, specifically the stability of different HA aggregates. The systems were progressively heated from 300 to 350 K.

2.2.2. Simulation Conditions. The structures of the two alternative HA models were first optimized at the B3LYP/def2-SV(P) level.²⁵ Optimized geometries were then submitted to the Automated Topology Builder (ATB) to obtain Lennard-Jones and bonded parameters compatible with the GROMOS 53A6 force field.^{26,27} Atomic charges were derived by fitting to the electrostatic potential using the CHELPG algorithm.²⁸ The IR spectra were simulated based on the optimized neutral HA structure at the B3LYP/6-31G(d) level using the Gaussian 09 program.^{29–31}

The GROMACS 5.0.7 simulation package was used to perform the MD simulations.^{32,33} Periodic boundary conditions (PBC) were applied in all dimensions. In the first three systems (I1A, N1, and I1B), the solutes were solvated in a cubic water box with a length of 5.0 nm. The extended simple point charge (SPC/E) water model was used,³⁴ and the excess negative charge was neutralized by Na^+ ions. After an initial steepest descent energy minimization, the system was equilibrated at a constant temperature, first with a canonical (NVT) ensemble for 100 ps by applying the v-rescale thermostat,³⁵ and then with an isothermal-isobaric (NPT) ensemble at 1 bar for another 100 ps using the Parrinello–Rahman barostat.³⁶ The coupling time of the thermostat (τ_T) and the barostat (τ_p) was 0.1 and 2.0 ps, respectively. Following this equilibration procedure, the system was sampled for 25 ns. Configurations from the trajectory were collected every 10 ps for the first 20 ns and every 0.01 ps for the last 5 ns for analysis. The first 20 ns were used to probe the spontaneous folding of HA and the last 5 ns were used to analyze the thermodynamic properties of the model systems. For the last three systems (I4, N4, and M4), following the 25 ns of sampling at 300 K described above, the systems were heated to 320 K for 5 ns, and then the temperature was increased to 350 K for an additional 25 ns of sampling (see Section S3 of SI). During the simulations, the LINCS algorithm was applied to constrain the lengths of all bonds.³⁷ The equations of motion were integrated using a time step of 2 fs. Electrostatic interactions were calculated using the particle mesh Ewald (PME) method.³⁸ Van der Waals (vdW) interactions were calculated using a cutoff of 1.4 nm. Trajectory analysis was performed using programs within the GROMACS package. VMD 1.9.1 was employed for visualization.³⁹ The Multiwfnn 3.3.9 program was used to localize and identify the noncovalent interaction (NCI),⁴⁰ which was introduced by Johnson et al.⁴¹

3. RESULTS AND DISCUSSION

3.1. Validation of the HA Model. The chemical composition of the purified HA was determined experimentally and the mass fractions of the elements C, H, and N were very close to those of the Stevenson model (see Section S1 of SI). The typical functional groups of HA, i.e., carboxylic, phenolic, carbonyl, and quinonol, are also well represented in the HA model used. Note, the content of N (1.16 wt %) is rather low in HA. This suggests that the hydrophilicity of HA is primarily determined by the Lewis acid sites rather than by the Lewis base sites. This was another reason why the amine group in our neutral model was treated as an uncharged polar group.

Furthermore, as shown in Figure 2, good agreement was observed between the FTIR spectrum of HA measured experimentally and the molecular vibrational frequencies calculated from the Stevenson model at the B3LYP/6-31G(d) level of theory with appropriate corrections.⁴² The deviations of all features were within 6%. The assignment of the characteristic peaks collected in Section S4 of SI is consistent with previous studies.^{43–49} The bond stretching modes of polar groups, including O–H and N–H stretching (3470 – $3527\ cm^{-1}$), O–H stretching involved in H-bond formation ($3268\ cm^{-1}$), and C=O stretching of COOH ($1740\ cm^{-1}$), and the bond stretching modes of apolar groups, such as the aromatic C–H stretching ($3095\ cm^{-1}$) and aliphatic C–H stretching ($2922\ cm^{-1}$), all agreed well with the corresponding experimental bands. The strong peak calculated

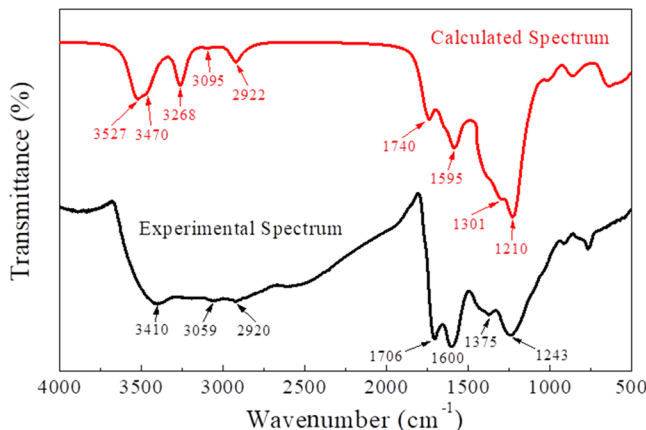


Figure 2. Experimental and calculated FTIR spectra of HA. The deviations of all features were within 6%.

to lie at about 1595 cm^{-1} , which corresponds to the experimental band at about 1600 cm^{-1} , is generally attributed to a combination of aromatic $\text{C}=\text{C}$ skeletal vibrations and the $\text{C}=\text{O}$ stretching of quinonol, amide, and H-bonded conjugated ketone groups. Overall, the consistency between the calculated results and the experimental data demonstrates that the model of HA proposed by Stevenson is appropriate in this case and was therefore used to study the dynamics of HA in an aqueous solution.

3.2. Folding of HA in the Aqueous Solution.

3.2.1. Folding. To investigate the folding of HA in an aqueous solution, MD simulations of the ionic (**I1A**, **I1B**) and neutral (**N1**) forms were performed at 300 and 350 K. The

representative snapshots of the three systems during the simulations are presented in Section S5 of SI. In all three systems, the two wings of HA came together, forming close contacts. The time evolution of different metrics was used to characterize the folding of HA, as shown in Figure 3. The solvent-accessible surface area (SASA), determined by the gmx-sasa program,⁵⁰ is shown in Figure 3a as a function of simulation time. It can be seen that the folding of HA from its extended conformation was accompanied by a decrease in its SASA. The behavior of NHA (**N1**) differs significantly from the two ionic forms of HA (**I1As**). Starting from extended conformation as well, NHA folded more slowly but eventually adopted a more compact conformation with a lower SASA value (13.42 nm^2). Figure 3b shows the free energy of solvation derived from the polar and nonpolar SASA ($\Delta G_{\text{solv},\text{SASA}}$) as a function of simulation time. The $\Delta G_{\text{solv},\text{SASA}}$ of NHA (1.62 kJ/mol) is noticeably more positive than the two I1As (-4.77 and -8.01 kJ/mol). This suggests that pH (the charge state) significantly affects the solubility of HA in water.

The positional root-mean-square deviation (RMSD) of backbone atoms (nonhydrogen atoms of structural units A, B, C, and D in Figure 1) from the starting structure, determined by the gmx-rms program, is another measure of structural change and folding dynamics during the simulation (Figure 3c). **N1** remained closer to the initial structure with a lower RMSD value at the end (0.56 nm), indicating that NHA has a less propensity to fold than I1A. The I1A at 350 K (**I1B**) showed more structural fluctuations than at a low temperature of 300 K (**I1A**), as expected. The compactness and stiffness of HA under different conditions were also

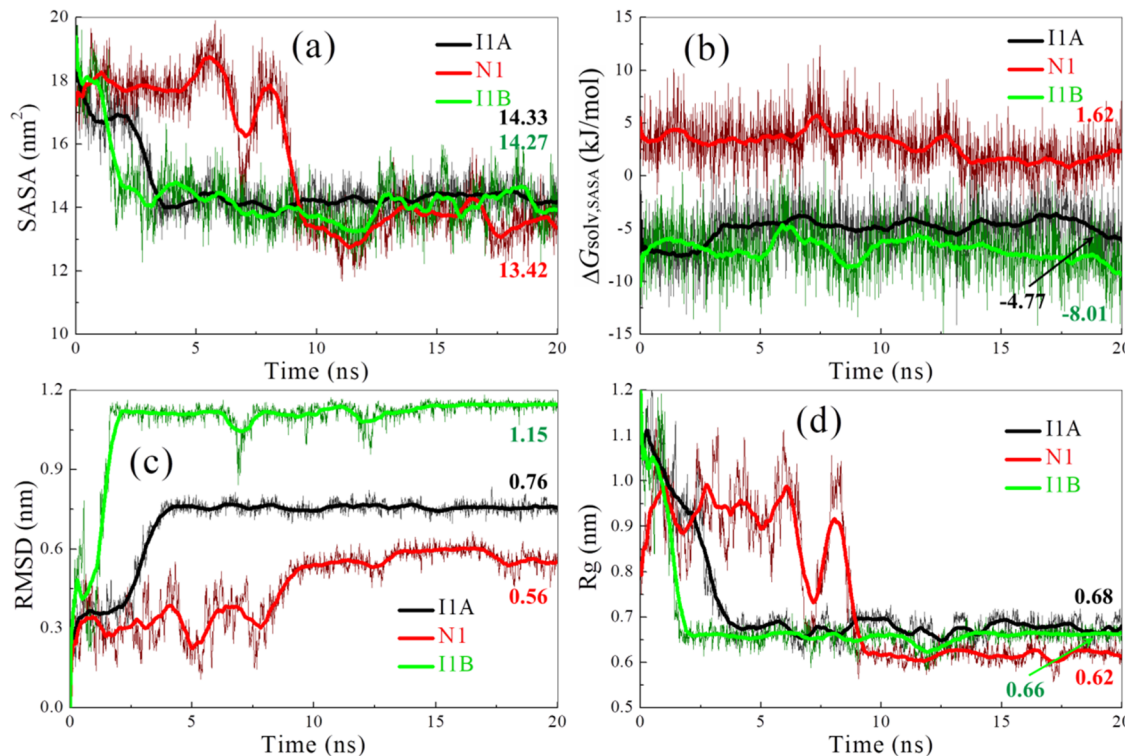


Figure 3. Time evolution of (a) solvent-accessible surface area (SASA), (b) free energy of solvation ($\Delta G_{\text{solv},\text{SASA}}$), (c) root-mean-square deviation (RMSD), and (d) radius of gyration (R_g) of HA in the **I1A**, **N1**, and **I1B** systems. Nonhydrogen atoms of structural units A, B, C, and D were chosen for RMSD and R_g calculations. The initially extended conformations (after energy minimization) were used as reference coordinates when calculating the RMSD. The values are averaged by the last 3 ns.

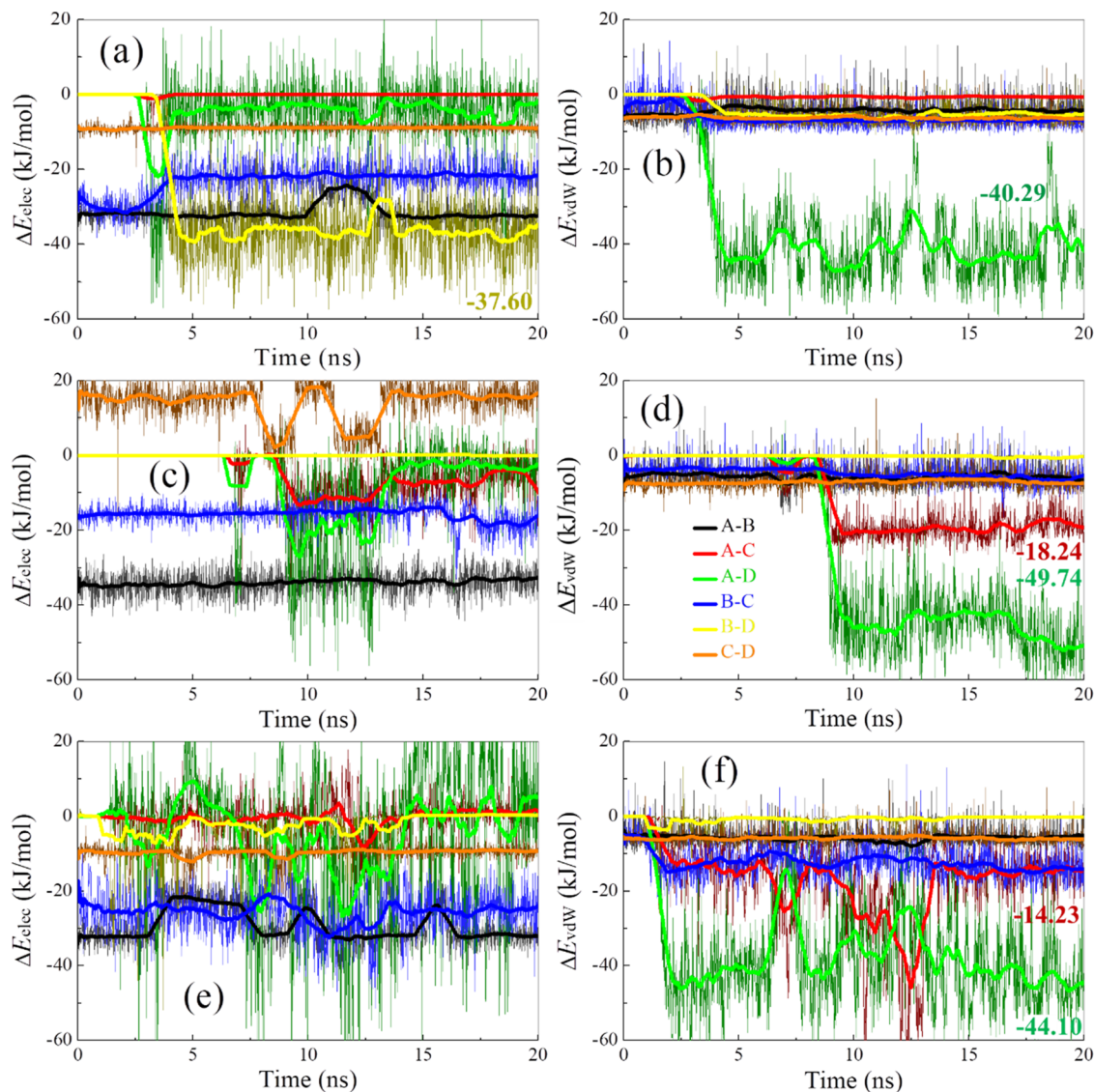


Figure 4. Time evolution of electrostatic (left) and vDW (right) interactions between the various units (A, B, C, and D) of HA in the IIA, N1, and IIB systems: (a, b) IIA, (c, d) N1, and (e, f) IIB. The legend of the curves is given in Figure 4d, and the values are averaged by the last 3 ns.

evaluated in terms of the radius of gyration (R_g) by the gmx-gyrate program (Figure 3d). A smaller R_g value represents a more compact conformation, and a less fluctuation of R_g in the time evolution indicates a relatively stable state. Upon the folding of HA, the R_g values decreased in all three systems, with the value of NHA (0.62 nm) slightly smaller than the two IHAs (0.66 and 0.68 nm). The R_g of NHA showed greater variation than the two ionic states (IHAs) during the first 9 ns. This was associated with the motion of the aromatic hydroxyl unit (unit D of HA, see Section S6 of SI). Overall, the results in Figure 3 suggest that HA had a strong propensity to fold spontaneously to a compact conformation in an aqueous solution, and the charge state of HA, as determined by the pH, significantly affects the folding of HA and consequently its conformation in the aqueous solution.

In addition, the folded state of HA was characterized using three descriptors ($V1$, $P1$, and $D1$), as shown in Figure 1, and the results are summarized in Section S7 of SI. The plots for $V1$ in the case of IIA, N1, and IIB show maxima at around 50° and a similar peak shape, suggesting a roughly collinear alignment of the two wings. However, for $P1$, substantial

differences were observed between the three systems, indicating that the flexibility of neutral HA was greater than when charged, which is consistent with the observations discussed above. The distributions of $D1$ are also significantly different, especially for $\alpha 2$ and $\alpha 3$, which is mainly due to the Tyr residue that bridged $\alpha 2$ and $\alpha 3$ and can rotate freely to adapt to the folding of HA. Overall, these findings suggest that HA is highly flexible and its folding modes are easily influenced by various external factors, such as pH (charge state) and temperature.

3.2.2. Energetic Analysis. The interaction energies between the different structure units (see Figure 1), which make up the HA model used in this work, i.e., the aromatic carboxylate (A), linker region (B), quinone (C), and aromatic hydroxyl (D), were analyzed by the gmx-energy program to understand the driving forces governing the spontaneous folding of HA in the IIA, N1, and IIB systems (Figure 4). In the case of ionized HA (IIA, Figure 4a,b), the electrostatic interactions between units B and D (-37.60 kJ/mol) and the vDW interactions between A and D (-40.29 kJ/mol) become significantly more favorable with the closing of the wings and likely drive the

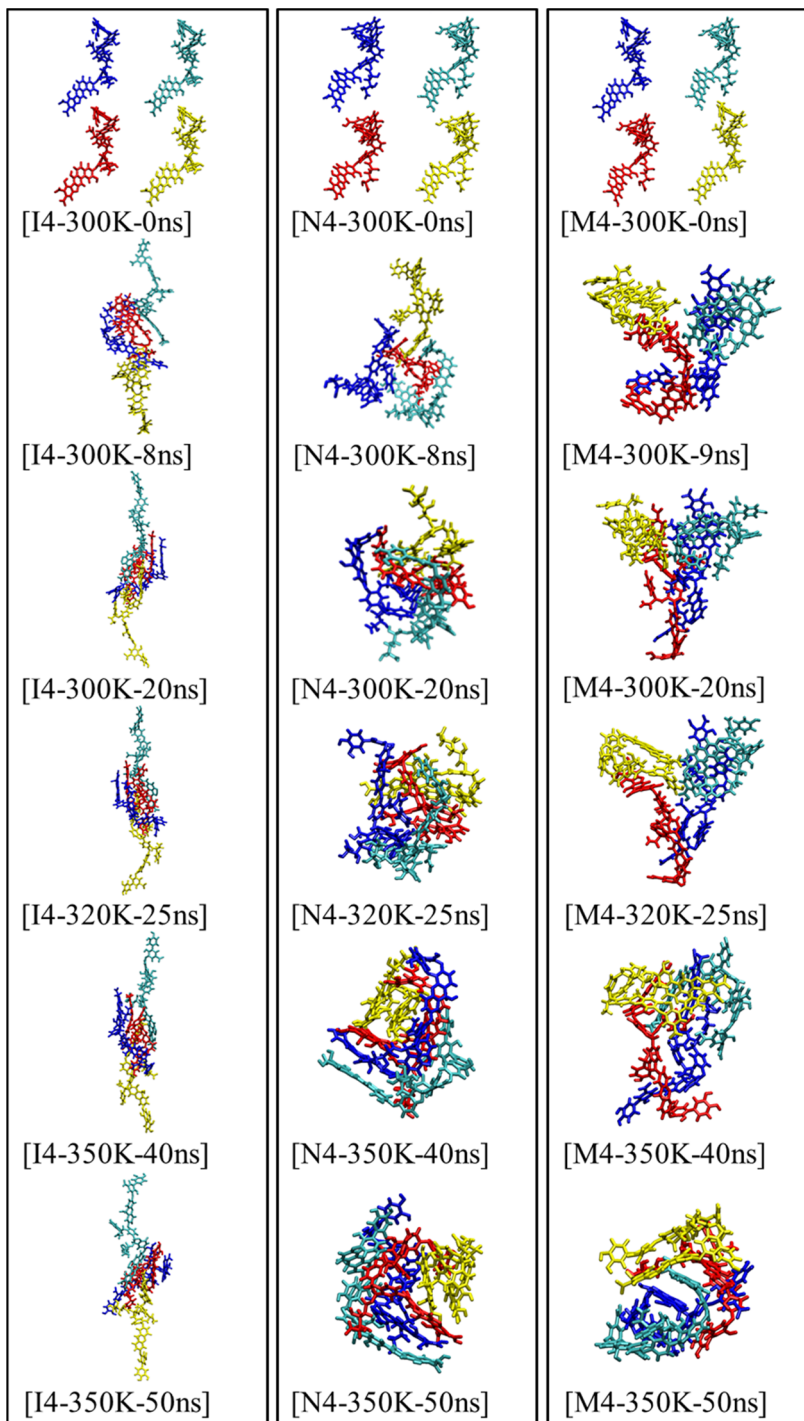


Figure 5. Representative snapshots of I4 (4 IHAs), N4 (4 NHAs), and M4 (2 NHAs and 2 IHAs) systems with increasing temperature from 300 to 350 K. Snapshots are labeled as X-yK-zns, representing the snapshot of the model system X ($X = \text{I4}$, N4 , and M4) at y kelvin and z th ns. The four HA molecules are distinguished by colors of red, cyan, blue, and yellow (specifically, for M4, red: NHA1; cyan: NHA2; blue: IHA1; yellow: IHA2). Water molecules are not shown for clarity. At high pH (I4), the ionized HAs assembled into a thread-like structure, while the neutral HAs formed a droplet-like aggregate at low pH (N4). The aggregate formed by two different charge states of HA appeared less stable and underwent a temperature-induced transition from a Y-shaped to a droplet-like structure (M4).

conformational change. In the neutral HA (N1, Figure 4c,d), the vdW interactions between A and D (-49.74 kJ/mol) and between A and C (-18.24 kJ/mol) appear to dictate folding. Similar results were observed at higher temperature (I1B, Figure 4e,f) where the vdW interactions are again dominant and essentially determine the folding of HA. In contrast, the changes in the electrostatics are still favorable in the N1 and

I1B systems but not as significant. Note, the time evolution of the electrostatic interactions in the case of N1 (Figure 4c) shows greater fluctuations than that in I1A (Figure 4a). This might reflect weaker electrostatic interactions in NHA. Similar cases can also be found in the case of I1B. The fluctuations in both electrostatic and vdW interactions are greater in I1B than those in I1A, suggesting an increase in the accessible

conformational space with increasing temperature. These results are consistent with the conformational analysis in Figure 3.

To further identify the interaction characteristics between the structural units of HA, noncovalent interaction (NCI) analysis was carried out based on the electron density and reduced density gradient.^{41,51} The gradient isosurfaces resulting from the analysis are shown in Section S8 of SI. It can be observed that the spaces between units A and D are mainly populated by green color (black ellipses), corresponding to $\pi-\pi$ interactions between the aromatic rings of A and D. Meanwhile, there is also intramolecular hydrogen bonding present in HA (demonstrated by some blue dots and highlighted by pink circles in Figure S6 of SI). After careful analysis of hydrogen bonding shown in Section S9 of SI, only a very few hydrogen bonds (0.04–0.22) formed between A and D during the simulations. These results indicated the copresence of electrostatics, vdW forces, $\pi-\pi$ interactions, and hydrogen bonding during the folding of HA, among which the vdW interactions between units A and D were the main driving force to govern its spontaneous folding.

3.3. Aggregation of HA in the Aqueous Solution.

3.3.1. Aggregation Kinetics: MD, DLS, and TEM. To examine how HA aggregates under different conditions, three systems (I4, N4, and M4) containing four HA molecules were prepared and simulated. Representative snapshots from the aggregation simulations are shown in Figure 5. In the I4 and N4 systems, the HA molecules aggregated rapidly with the aggregates remaining stable even if heated to 350 K for 25 ns. However, in the M4 system, the aggregates that formed at 300 K first disassociated then reassociated at a higher temperature (350 K). From Figure 5, one can see that, depending on the charge state of HA (ionic vs neutral), different aggregates were formed. I4 formed a thread-like structure, while the N4 aggregate was more of a droplet. Previous studies have shown that in an alkaline solution, ionic HA forms linear and/or sheet-like aggregates, whereas globular and ring-like structures are formed under an acidic condition where HA is in a neutral state.^{52,53} In the M4 system that contained two different charge states of HA, the aggregates appeared less stable and underwent a temperature-induced transition from a Y-shaped to droplet-like aggregate.

To shed further light on the nature of the structures forming the aggregates, each 50 ns trajectory starting from the point where all HA molecules were in an extended conformation was subjected to cluster analysis based on the difference in positional RMSD using the method of Daura et al.⁵⁴ Here, all nonhydrogen atoms were considered when calculating the RMS and the cluster threshold was 0.1 nm. The dominant conformational clusters from each simulation are provided in Section S10 of SI. In the I4 and N4 systems, the conformations of the individual HA molecules changed little during the simulations. However, in the M4 system, multiple clusters of HA conformations were observed with the conformations of some molecules changing greatly during the simulation with increasing temperature. For instance, IHAA1 transformed from an extended conformation at 300 K to a folded one at 350 K. These structural changes of each HA molecule resulted in the temperature-induced transition from a Y-shaped structure to a droplet-like aggregate, as shown in Figure 5.

The aggregation of HA molecules under acidic (pH 2.5) and near-neutral (pH 7.8) solutions was characterized experimentally using DLS measurements to determine the average

hydrodynamic diameter ($\langle D_h \rangle$). The results obtained are shown in Figure 6a. At pH 2.5, as expected, the size of the HA

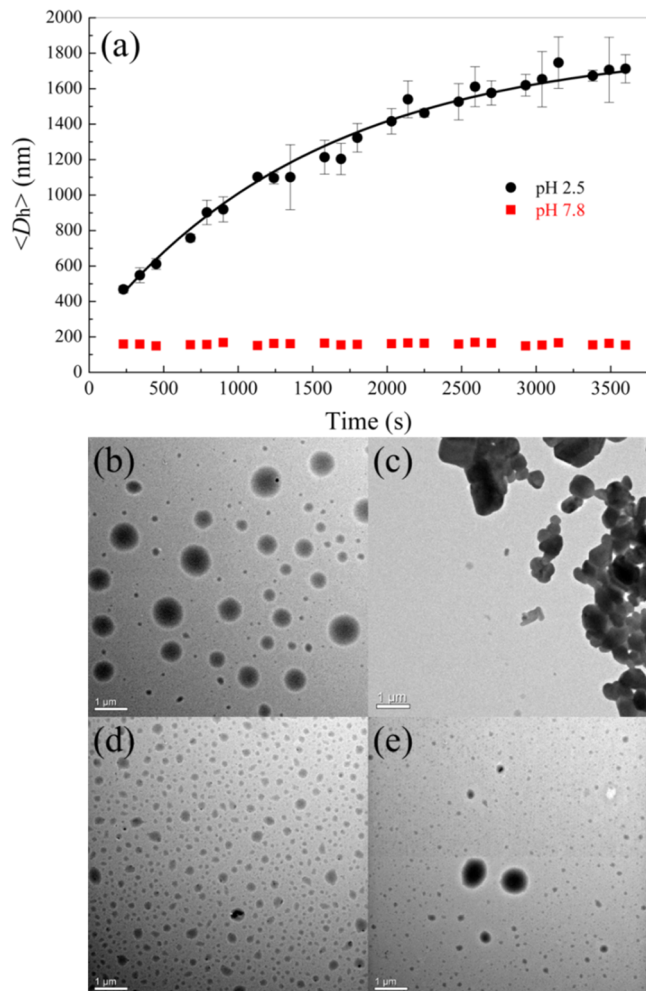


Figure 6. (a) Aggregation kinetic profiles of HAs (50 mg/L) at pH 2.5 and 7.8 as a function of time and TEM images of the HA aggregates at time $t = 0$ (left) and 12 h (right) under different pH values: (b, c) pH 2.5 and (d, e) pH 7.8.

aggregates increased progressively from ~460 to ~1700 nm over a period of an hour. Observed over longer time scales, some precipitates were visible within 24 h with a flocculent forming within 4 days (see Section S11 of SI). By comparison, at pH 7.8, the size of the aggregate (~160 nm) changed little over the first hour and little to no precipitation was observed after 4 days. We note that the size of ~160 nm is significantly larger than that of the aggregates observed in MD simulations. This is due to the distinct time and spatial scales, which is 50 ns scale and molecular scale in MD simulations, while hour-to-days scale and macroscopic scale in experimental studies. Figure 6b–e shows TEM images of the HA aggregates at $t = 0$ and 12 h under acidic (pH 2.5) and near-neutral (pH 7.8) conditions. Initially ($t = 0$ h, Figure 6b,d), the HA aggregates were well dispersed but with the HA aggregates at pH 2.5 being visibly larger than those at pH 7.8, in accord with the $\langle D_h \rangle$ measured by DLS. A previous study has shown that some small single particles or aggregates can be found on the surface of mica by atomic force microscopy (AFM) in an initial state of HA aggregation at pH 4.0,⁵⁵ which is consistent with the morphology observed at the initial time in our TEM imaging.

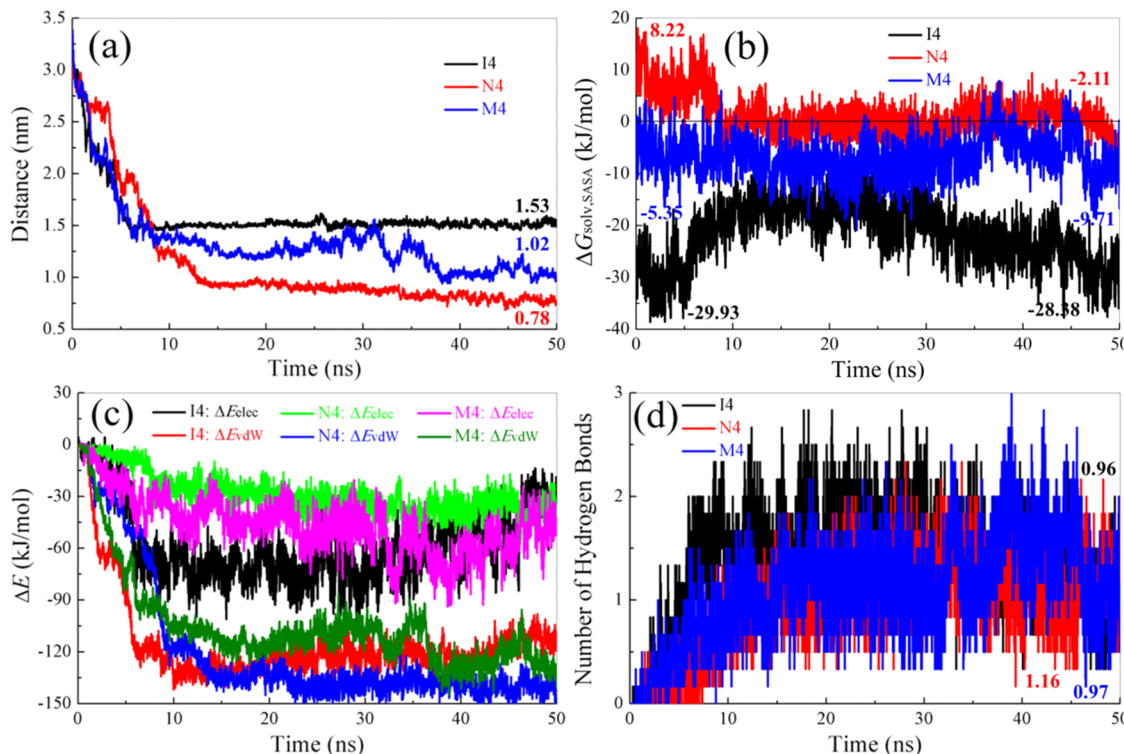


Figure 7. Time evolution of (a) average COG distance between the various HAs, (b) total free energy of solvation ($\Delta G_{\text{solv},\text{SASA}}$) of four HAs, (c) average electrostatic and vdW interactions, and (d) average number of hydrogen bonds between the HA molecules in the I4, N4, and M4 systems. The values are averaged by initial or last 3 ns.

After 12 h, at pH 2.5, globular aggregates formed large particle-like structures adjacent to each other with smooth peripheries (Figure 6c). These higher-order collective structures were not seen at pH 7.8 (Figure 6e).⁵⁶ These results demonstrated that the aggregation extent of HA decreased significantly with increasing pH. Clearly, the solution pH affects not only the size and shape of individual aggregates but also the formation of larger assemblies, consistent with observations from our MD simulations. We note that the droplet- and thread-like structures were not observed in TEM images, which may be overlooked due to the spatiotemporal resolution. This demonstrates how the present MD study complements experiments.

3.3.2. Aggregation Mechanism. The average distances between the center of geometry (COG) of each pair of HAs in the three systems were calculated by the gmx-distance program to analyze the compactness of the HA aggregates. As shown in Figure 7a, the average COG distance of HA pairs in I4 (1.53 nm) is much larger than that in N4 (0.78 nm), indicating that the neutral aggregates are more compact. In addition, during the last 25 ns of the M4 system, the average COG distance first increased and then decreased as the temperature was increased to 350 K, supporting the finding that the initial aggregate partly disassociated before reassociating into a more compact structure. Figure 7b shows the free energy of solvation as a function of time in the aggregation simulations. Again, the free energy of solvation was estimated based on the SASA ($\Delta G_{\text{solv},\text{SASA}}$). It is important to note, when examining Figure 7b, that the key property, which determines the tendency of the system to aggregate is not the free energy of solvation of the individual HA molecules but the difference in the free energy of the system between the aggregated and non-aggregated forms. In addition to the solvation contributions of

the individual HA molecules included in the $\Delta G_{\text{solv},\text{SASA}}$ values, the total free energy of the system involves enthalpic contributions from the interactions of HA–HA, HA–water, and water–water molecules. Thus, while the $\Delta G_{\text{solv},\text{SASA}}$ values provide a useful estimate of the main contributions to solvation, the values should not be over interpreted. In the case of N4, $\Delta G_{\text{solv},\text{SASA}}$ of the four NHAs was positive (8.22 kJ/mol) before aggregation, suggesting they had little tendency to interact with or disperse in water. After forming a droplet-like aggregate, the total free energy of solvation was negative (-2.11 kJ/mol). In the case of M4 and I4, aggregation was observed despite the free energy of solvation being negative before aggregation (-9.71 kJ/mol for M4; -28.38 kJ/mol for I4). Indeed, in the case of I4, the free energy of solvation initially became less negative (-29.93 kJ/mol), suggesting that at least in terms of the solvation contribution, aggregate formation was unfavorable. In this case, aggregation is likely driven by electrostatic, vdW, and hydrogen-bonding interactions between the HA molecules.

The intermolecular energy of interaction is shown in Figure 7c, and the number of hydrogen bonds determined by the gmx-hbond program is shown in Figure 7d. In all three systems, the vdW interactions dominate but are of a similar magnitude so do not account for the differences observed. However, the electrostatic interaction in I4 is significantly larger than that in N4. This could explain how the aggregate can form despite an unfavorable change in the free energy of solvation. The balance between solvation and electrostatic interactions between the HA molecules can explain how the I4 system could expand and contract. Again, this is consistent with the experimental results shown in Figure 6, suggesting that HA is more soluble in a near-neutral as opposed to an acidic solution. The analysis of the hydrogen-bonding

interactions revealed that once aggregated, the average number of intermolecular hydrogen bonds between HA pairs in I4 (0.96), N4 (1.16), and M4 (0.97) was roughly the same, suggesting that hydrogen bonding contributed a little to the aggregation of HAs.

3.4. Environmental Implications. A range of new insights into the behavior of HA in the aqueous phase together with a molecular-level understanding of the relationship between the pH environment and the structure, solubility, and aggregation of HA is well presented in this study. The solution pH was known to be a determining factor in the extent of HA aggregation, which was confirmed by MD simulations, DLS measurements, and TEM imaging. Ionized HA molecules (representing near-neutral pH) were observed to assemble into a thread-like structure, whereas neutral HA molecules (representing acidic pH) formed droplet-like aggregates. This behavior could be rationalized in terms of differences in the nature of the interatomic interactions and solvation effects, specifically the decreased hydrophilicity due to the protonation of the widely distributed carboxylate groups.

Understanding the molecular details of the pH-dependent aggregation of HA has direct implications on the remediation of sites contaminated by heavy metal ions and even radionuclides. The remediation of these sites requires the removal of metal ions. These cations form stable hydrated complexes in the aqueous phase.^{57,58} They can be sequestered using chelating reagents that either form inner-shell coordination complexes via ligand exchange or by the formation of outer-shell coordination complexes in which the hydrated metal ion complex is encapsulated.^{59,60} In principle, HA is able to participate via both mechanisms as it contains a variety of functional groups capable of coordinating directly with metal ions, as well as forming aggregates containing a wide range of pores where a variety of ions and other complexes can be trapped.^{14,61}

Indeed, in soil, HA aggregates are expected to form a complex composite material including small inorganic ions, e.g., chloride, carbonate anions, and organic ligands such as fulvic acid, which could further enhance the ability to trap heavy metal complexes. In contrast, at high pH, the hydrophilicity of the HAs is enhanced, exposing charged carboxylate groups, which can directly coordinate with the ions of heavy metals. However, as the propensity for HA to aggregate at near-neutral pH is lower, although the metal ions would be more tightly bound to HA, the overall rate at which ions might migrate through the system may well be greater.^{62–64} The form of HA in groundwater is believed to affect the ability of HA to bind to and transport heavy metal ions, and so groundwater pH could potentially be used to modulate HA-based remediation strategies of contaminated sites.

■ ASSOCIATED CONTENT

§ Supporting Information

The Supporting Information is available free of charge at <https://pubs.acs.org/doi/10.1021/acs.est.1c05938>.

Chemical compositions of HA, compositions and key parameters of the simulated systems, temperature, assignment of the characteristic peaks in FTIR spectra, representative snapshots, RMSD, nature of the folded state, noncovalent interaction (NCI) analysis, hydrogen

bonds, clustering analysis, photographs of HA aggregates, M4 system, significance of this work and its difference with the others published, and reason to use the Stevenson HA model ([PDF](#))

■ AUTHOR INFORMATION

Corresponding Authors

Alan E. Mark – School of Chemistry & Molecular Biosciences, The University of Queensland, St. Lucia, QLD 4072, Australia; [orcid.org/0000-0001-5880-4798](#); Email: a.e.mark@uq.edu.au

Ning Liu – Key Laboratory of Radiation Physics and Technology of the Ministry of Education, Institute of Nuclear Science and Technology, Sichuan University, Chengdu 610064, P. R. China; [orcid.org/0000-0003-2835-8066](#); Email: nliu720@scu.edu.cn

Dongqi Wang – School of Chemical Engineering, Dalian University of Technology, Dalian 116024, P. R. China; [orcid.org/0000-0001-9415-1173](#); Email: wangdq@dlut.edu.cn

Authors

Tu Lan – Key Laboratory of Radiation Physics and Technology of the Ministry of Education, Institute of Nuclear Science and Technology, Sichuan University, Chengdu 610064, P. R. China; [orcid.org/0000-0002-9877-2636](#)

Peng Wu – Key Laboratory of Radiation Physics and Technology of the Ministry of Education, Institute of Nuclear Science and Technology, Sichuan University, Chengdu 610064, P. R. China

Ziyi Liu – School of Chemical Engineering, Dalian University of Technology, Dalian 116024, P. R. China; [orcid.org/0000-0003-1616-7537](#)

Martin Stroet – School of Chemistry & Molecular Biosciences, The University of Queensland, St. Lucia, QLD 4072, Australia

Jiali Liao – Key Laboratory of Radiation Physics and Technology of the Ministry of Education, Institute of Nuclear Science and Technology, Sichuan University, Chengdu 610064, P. R. China

Zhifang Chai – State Key Laboratory of Radiation Medicine and Protection, and School for Radiological and Interdisciplinary Sciences (RAD-X), Soochow University, Suzhou 215123, P. R. China

Complete contact information is available at: <https://pubs.acs.org/10.1021/acs.est.1c05938>

Notes

The authors declare no competing financial interest.

■ ACKNOWLEDGMENTS

This work was financially supported by the National Natural Science Foundation of China (Grant Nos. 22106111, 21473206), the LiaoNing Revitalization Talents Program (XLYC2002015), and the Fundamental Research Funds for the Central Universities. Calculations were done on the computational grids at the National Supercomputing Center in Tianjin (NSCC-TJ).

■ REFERENCES

- (1) Stevenson, F. J. *Humus Chemistry: Genesis, Composition, Reactions*; John Wiley & Sons: New York, 1994; pp 1–56.

- (2) Aiken, G. R.; McKnight, D. M.; Wershaw, R. L.; MacCarthy, P. *Humic Substances in Soil, Sediment, and Water: Geochemistry, Isolation, and Characterization*; John Wiley & Sons: New York, 1985; pp 493–582.
- (3) Trout, C. C.; Kubicki, J. D. Molecular modeling of Al³⁺ and benzene interactions with Suwannee fulvic acid. *Geochim. Cosmochim. Acta* **2007**, *71*, 3859–3871.
- (4) Aristilde, L.; Sposito, G. Binding of ciprofloxacin by humic substances: A molecular dynamics study. *Environ. Toxicol. Chem.* **2010**, *29*, 90–98.
- (5) Jebali, A.; Behzadi, A.; Rezapor, I.; Jasemizad, T.; Hekmatmoghadam, S. H.; Halvani, G. H.; Sedighi, N. Adsorption of humic acid by amine-modified nanocellulose: An experimental and simulation study. *Int. J. Environ. Sci. Technol.* **2015**, *12*, 45–52.
- (6) Sadhu, B.; Sundararajan, M.; Bandyopadhyay, T. Water-mediated differential binding of strontium and cesium cations in fulvic acid. *J. Phys. Chem. B* **2015**, *119*, 10989–10997.
- (7) Wu, G.; Zhu, X.; Ji, H.; Chen, D. Molecular modeling of interactions between heavy crude oil and the soil organic matter coated quartz surface. *Chemosphere* **2015**, *119*, 242–249.
- (8) Zhou, X.; Wang, B.; Lan, T.; Chen, H.; Wang, H.; Tao, Y.; Li, Z.; Ibrahim, K.; Wang, D.; Feng, W. Chirality of graphene oxide-humic acid sandwich complex induced by a twisted, long-range-ordered nanostructure. *J. Phys. Chem. C* **2016**, *120*, 25789–25795.
- (9) Tan, L.; Tan, X.; Mei, H.; Ai, Y.; Sun, L.; Zhao, G.; Hayat, T.; Alsaedi, A.; Chen, C.; Wang, X. Coagulation behavior of humic acid in aqueous solutions containing Cs⁺, Sr²⁺ and Eu³⁺: DLS, EEM and MD simulations. *Environ. Pollut.* **2018**, *236*, 835–843.
- (10) Tan, L.; Yu, Z.; Tan, X.; Fang, M.; Wang, X.; Wang, J.; Xing, J.; Ai, Y.; Wang, X. Systematic studies on the binding of metal ions in aggregates of humic acid: Aggregation kinetics, spectroscopic analyses and MD simulations. *Environ. Pollut.* **2019**, *246*, 999–1007.
- (11) Petrov, D.; Tunega, D.; Gerzabek, M. H.; Oostenbrink, C. Molecular modelling of sorption processes of a range of diverse small organic molecules in Leonardite humic acid. *Eur. J. Soil Sci.* **2020**, *71*, 831–844.
- (12) Gotsmay, M.; Escalona, Y.; Oostenbrink, C.; Petrov, D. Exploring the structure and dynamics of proteins in soil organic matter. *Proteins: Struct., Funct., Bioinf.* **2021**, *89*, 925–936.
- (13) Lan, T.; Wang, H.; Liao, J.; Yang, Y.; Chai, Z.; Liu, N.; Wang, D. Dynamics of humic acid and its interaction with uranyl in the presence of hydrophobic surface implicated by molecular dynamics simulations. *Environ. Sci. Technol.* **2016**, *50*, 11121–11128.
- (14) Lan, T.; Liao, J.; Yang, Y.; Chai, Z.; Liu, N.; Wang, D. Competition/cooperation between humic acid and graphene oxide in uranyl adsorption implicated by molecular dynamics simulations. *Environ. Sci. Technol.* **2019**, *53*, 5102–5110.
- (15) Zhu, X.; Chen, D.; Wu, G. Molecular dynamic simulation of asphaltene co-aggregation with humic acid during oil spill. *Chemosphere* **2015**, *138*, 412–421.
- (16) Sündermann, A.; Solc, R.; Tunega, D.; Haberhauer, G.; Gerzabek, M. H.; Oostenbrink, C. Vienna Soil-Organic-Matter Modeler—Generating condensed-phase models of humic substances. *J. Mol. Graphics Modell.* **2015**, *62*, 253–261.
- (17) Escalona, Y.; Petrov, D.; Oostenbrink, C. Vienna soil organic matter modeler 2 (VSOMM2). *J. Mol. Graphics Modell.* **2021**, *103*, No. 107817.
- (18) Petrov, D.; Tunega, D.; Gerzabek, M. H.; Oostenbrink, C. Molecular dynamics simulations of the standard leonardite humic acid: Microscopic analysis of the structure and dynamics. *Environ. Sci. Technol.* **2017**, *51*, 5414–5424.
- (19) Diallo, M. S.; Simpson, A.; Gassman, P.; Faulon, J. L.; Johnson, J. H.; Goddard, W. A.; Hatcher, P. G. 3-D structural modeling of humic acids through experimental characterization, computer assisted structure elucidation and atomistic simulations. 1. Chelsea soil humic acid. *Environ. Sci. Technol.* **2003**, *37*, 1783–1793.
- (20) Porquet, A.; Bianchi, L.; Stoll, S. Molecular dynamic simulations of fulvic acid clusters in water. *Colloids Surf., A* **2003**, *217*, 49–54.
- (21) Sutton, R.; Sposito, G.; Diallo, M. S.; Schulten, H. R. Molecular simulation of a model of dissolved organic matter. *Environ. Toxicol. Chem.* **2005**, *24*, 1902–1911.
- (22) Alvarez-Puebla, R. A.; Valenzuela-Calahorro, C.; Garrido, J. J. Theoretical study on fulvic acid structure, conformation and aggregation: A molecular modelling approach. *Sci. Total Environ.* **2006**, *358*, 243–254.
- (23) Mobed, J. J.; Hemmingsen, S. L.; Autry, J. L.; McGown, L. B. Fluorescence characterization of IHSS humic substances: Total luminescence spectra with absorbance correction. *Environ. Sci. Technol.* **1996**, *30*, 3061–3065.
- (24) Wei, M.; Liao, J.; Liu, N.; Zhang, D.; Kang, H.; Yang, Y.; Yang, Y.; Jin, J. Interaction between uranium and humic acid (I): Adsorption behaviors of U(VI) in soil humic acids. *Nucl. Sci. Tech.* **2007**, *18*, 287–293.
- (25) Schäfer, A.; Horn, H.; Ahlrichs, R. Fully optimized contracted Gaussian basis sets for atoms Li to Kr. *J. Chem. Phys.* **1992**, *97*, 2571–2577.
- (26) Oostenbrink, C.; Villa, A.; Mark, A.; van Gunsteren, W. A biomolecular force field based on the free enthalpy of hydration and solvation: the GROMOS force-field parameter sets 53A5 and 53A6. *J. Comput. Chem.* **2004**, *25*, 1656–1676.
- (27) Malde, A. K.; Zuo, L.; Breeze, M.; Stroet, M.; Poger, D.; Nair, P. C.; Oostenbrink, C.; Mark, A. E. An automated force field topology builder (ATB) and repository: Version 1.0. *J. Chem. Theory Comput.* **2011**, *7*, 4026–4037.
- (28) Breneman, C.; Wiberg, K. Determining atom-centered monopoles from molecular electrostatic potentials. The need for high sampling density in formamide conformational analysis. *J. Comput. Chem.* **1990**, *11*, 361–373.
- (29) Hariharan, P. C.; Pople, J. A. The influence of polarization functions on molecular orbital hydrogenation energies. *Theor. Chim. Acta* **1973**, *28*, 213–222.
- (30) Becke, A. D. A new mixing of Hartree-Fock and local density-functional theories. *J. Chem. Phys.* **1993**, *98*, 1372–1377.
- (31) Frisch, M. J.; Trucks, G. W.; Schlegel, H. B.; Scuseria, G. E.; Robb, M. A.; Cheeseman, J. R.; Scalmani, G.; Barone, V.; Mennucci, B.; Petersson, G. A.; Nakatsuji, H.; Caricato, M.; Li, X.; Hratchian, H. P.; Lzmaylov, A. F.; Bloino, J.; Zheng, G.; Sonnenberg, J. L.; Hada, M.; Ehara, M.; Toyota, K.; Fukuda, R.; Hasegawa, J.; Ishida, M.; Nakajima, T.; Honda, Y.; Kitao, O.; Nakai, H.; Vreven, T.; Montgomery, J. A., Jr.; Peralta, J. E.; Ogliaro, F.; Bearpark, M.; Heyd, J. J.; Brothers, E.; Kudin, K. N.; Staroverov, V. N.; Kobayashi, R.; Normand, J.; Raghavachari, K.; Rendell, A.; Burant, J. C.; Liyengar, S. S.; Tomasi, J.; Cossi, M.; Rega, N.; Millam, J. M.; Klene, M.; Knox, J. E.; Cross, J. B.; Bakken, V.; Adamo, C.; Jaramillo, J.; Gomperts, R.; Stratmann, R. E.; Yazev, O.; Austin, A. J.; Cammi, R.; Pomelli, C.; Ochterski, J. W.; Martin, R. L.; Morokuma, K.; Zakrzewski, V. G.; Voth, G. A.; Salvador, P.; Dannenberg, J. J.; Dapprich, S.; Daniels, A. D.; Farkas, O.; Foresman, J. B.; Ortiz, J. V.; Cioslowski, J.; Fox, D. J. *Gaussian 09*; Gaussian, Inc.: Wallingford, CT, 2009.
- (32) Pronk, S.; Páll, S.; Schulz, R.; Larsson, P.; Bjelkmar, P.; Apostolov, R.; Shirts, M. R.; Smith, J. C.; Kasson, P. M.; van der Spoel, D.; Hess, B.; Lindahl, E. GROMACS 4.5: A high-throughput and highly parallel open source molecular simulation toolkit. *Bioinformatics* **2013**, *29*, 845–854.
- (33) Abraham, M. J.; Murtola, T.; Schulz, R.; Páll, S.; Smith, J. C.; Hess, B.; Lindahl, E. GROMACS: High performance molecular simulations through multi-level parallelism from laptops to supercomputers. *SoftwareX* **2015**, *1–2*, 19–25.
- (34) Berendsen, H. J. C.; Grigera, J. R.; Straatsma, T. P. The missing term in effective pair potentials. *J. Phys. Chem. A* **1987**, *91*, 6269–6271.
- (35) Bussi, G.; Donadio, D.; Parrinello, M. Canonical sampling through velocity rescaling. *J. Chem. Phys.* **2007**, *126*, No. 014101.
- (36) Parrinello, M.; Rahman, A. Polymorphic transitions in single crystals: A new molecular dynamics method. *J. Appl. Phys.* **1981**, *S2*, 7182–7190.

- (37) Hess, B. P-LINCS: A parallel linear constraint solver for molecular simulation. *J. Chem. Theory Comput.* **2008**, *4*, 116–122.
- (38) Essmann, U.; Perera, L.; Berkowitz, M. L.; Darden, T.; Lee, H.; Pedersen, L. G. A smooth particle mesh Ewald method. *J. Chem. Phys.* **1995**, *103*, 8577–8593.
- (39) Humphrey, W.; Dalke, A.; Schulten, K. VMD: Visual molecular dynamics. *J. Mol. Graphics* **1996**, *14*, 33–38.
- (40) Lu, T.; Chen, F. Multiwfn: A multifunctional wavefunction analyzer. *J. Comput. Chem.* **2012**, *33*, 580–592.
- (41) Johnson, E. R.; Keinan, S.; Mori-Sanchez, P.; Contreras-Garcia, J.; Cohen, A. J.; Yang, W. Revealing noncovalent interactions. *J. Am. Chem. Soc.* **2010**, *132*, 6498–6506.
- (42) Merrick, J. P.; Moran, D.; Radom, L. An evaluation of harmonic vibrational frequency scale factors. *J. Phys. Chem. A* **2007**, *111*, 11683–11700.
- (43) Schepetkin, I. A.; Khlebnikov, A. I.; Ah, S. Y.; Woo, S. B.; Jeong, C. S.; Klubachuk, O. N.; Kwon, B. S. Characterization and biological activities of humic substances from mumie. *J. Agric. Food Chem.* **2003**, *51*, 5245–5254.
- (44) Li, L.; Zhao, Z.; Huang, W.; Peng, P.; Sheng, G.; Fu, J. Characterization of humic acids fractionated by ultrafiltration. *Org. Geochem.* **2004**, *35*, 1025–1037.
- (45) Trompowsky, P. M.; Benites, V. D.; Madari, B. E.; Pimenta, A. S.; Hockaday, W. C.; Hatcher, P. G. Characterization of humic like substances obtained by chemical oxidation of eucalyptus charcoal. *Org. Geochem.* **2005**, *36*, 1480–1489.
- (46) Shirshova, L. T.; Ghabbour, E. A.; Davies, G. Spectroscopic characterization of humic acid fractions isolated from soil using different extraction procedures. *Geoderma* **2006**, *133*, 204–216.
- (47) Kim, H.-C.; Yu, M.-J. Characterization of aquatic humic substances to DBPs formation in advanced treatment processes for conventionally treated water. *J. Hazard. Mater.* **2007**, *143*, 486–493.
- (48) He, M. C.; Shi, Y. H.; Lin, C. Y. Characterization of humic acids extracted from the sediments of the various rivers and lakes in China. *J. Environ. Sci.* **2008**, *20*, 1294–1299.
- (49) Esteves, V. I.; Otero, M.; Duarte, A. C. Comparative characterization of humic substances from the open ocean, estuarine water and fresh water. *Org. Geochem.* **2009**, *40*, 942–950.
- (50) Eisenhaber, F.; Lijnzaad, P.; Argos, P.; Sander, C.; Scharf, M. The double cubic lattice method: Efficient approaches to numerical integration of surface area and volume and to dot surface contouring of molecular assemblies. *J. Comput. Chem.* **1995**, *16*, 273–284.
- (51) Lan, T.; Zeng, H.; Tang, T. Understanding adsorption of violanthrone-79 as a model asphaltene compound on quartz surface using molecular dynamics simulations. *J. Phys. Chem. C* **2018**, *122*, 28787–28796.
- (52) Myneni, S. C. B.; Brown, J. T.; Martinez, G. A.; Meyer-Ilse, W. Imaging of humic substance macromolecular structures in water and soils. *Science* **1999**, *286*, 1335–1337.
- (53) Chen, Y.; Schnitzer, M. Scanning electron microscopy of a humic acid and of a fulvic acid and its metal and clay complexes. *Soil Sci. Soc. Am. J.* **1976**, *40*, 682–686.
- (54) Daura, X.; van Gunsteren, W. F.; Mark, A. E. Folding-unfolding thermodynamics of a β -heptapeptide from equilibrium simulations. *Proteins: Struct., Funct., Bioinf.* **1999**, *34*, 269–280.
- (55) Plaschke, M.; Römer, J.; Klenze, R.; Kim, J. I. In situ AFM study of sorbed humic acid colloids at different pH. *Colloids Surf., A* **1999**, *160*, 269–279.
- (56) Baalousha, M.; Motelica-Heino, M.; Galaup, S.; Le Coustumer, P. Supramolecular structure of humic acids by TEM with improved sample preparation and staining. *Microsc. Res. Tech.* **2005**, *66*, 299–306.
- (57) Persson, I. Hydrated metal ions in aqueous solution: How regular are their structures? *Pure Appl. Chem.* **2010**, *82*, 1901–1917.
- (58) Jakubowska, A. Bonding stability and dehydration constants for hydrated metal ions. *J. Chem. Eng. Data* **2010**, *55*, 1876–1881.
- (59) Sverjensky, D. A.; Fukushi, K. A predictive model (ETLM) for As(III) adsorption and surface speciation on oxides consistent with spectroscopic data. *Geochim. Cosmochim. Acta* **2006**, *70*, 3778–3802.
- (60) Pankhurst, J. R.; Bell, N. L.; Zegke, M.; Platts, L. N.; Lamfsus, C. A.; Maron, L.; Natrajan, L. S.; Sproules, S.; Arnold, P. L.; Love, J. B. Inner-sphere vs. outer-sphere reduction of uranyl supported by a redox-active, donor-expanded dipyrin. *Chem. Sci.* **2017**, *8*, 108–116.
- (61) Lindoy, L. F. Outer-sphere and inner-sphere complexation of cations by the natural ionophore lasalocid A. *Coord. Chem. Rev.* **1996**, *148*, 349–368.
- (62) Reiller, P.; Casanova, F.; Moulin, V. Influence of addition order and contact time on thorium(IV) retention by hematite in the presence of humic acids. *Environ. Sci. Technol.* **2005**, *39*, 1641–1648.
- (63) Pan, D.; Fan, Q.; Li, P.; Liu, S.; Wu, W. Sorption of Th(IV) on Na-bentonite: Effects of pH, ionic strength, humic substances and temperature. *Chem. Eng. J.* **2011**, *172*, 898–905.
- (64) Yang, J.; Ge, M.; Jin, Q.; Chen, Z.; Guo, Z. Co-transport of U(VI), humic acid and colloidal gibbsite in water-saturated porous media. *Chemosphere* **2019**, *231*, 405–414.